ACS OMEGA

http://pubs.acs.org/journal/acsodf

Article

Efficient Photocatalytic Dye Degradation and Bacterial Inactivation by Graphitic Carbon Nitride and Starch-Doped Magnesium Hydroxide Nanostructures

Muhammad Ikram,* Farzana Jamal, Ali Haider, Sobia Dilpazir, Tahira Shujah, Misbah Naz, Muhammad Imran, Anwar Ul-Hamid, Iram Shahzadi, Hassam Ullah, Walid Nabgan,* and Salamat Ali

Cite This: *ACS Omega* 2022, 7, 39998−40008

Read Online

ACCESS | Metrics & More | Article Recommendations

ABSTRACT: The removal of hazardous pollutants from water is becoming an increasingly interesting topic of research considering their impact on the environment and the ecosystem. This work was carried out to synthesize graphitic carbon nitride (g-C_3N_4) and starch-doped magnesium hydroxide (g-C_3N_4/St-$Mg(OH)_2$) nanostructures via a facile co-precipitation process. The focus of this study is to treat polluted water and bactericidal behavior with a ternary system (doping-dependent $Mg(OH)_2$). Different concentrations (2 and 4 wt %) of g-C_3N_4 were doped in a fixed amount of starch and $Mg(OH)_2$ to degrade methylene blue dye from an aqueous solution with bactericidal potential against *Escherichia coli* (*E. coli*) and *Staphylococcus aureus* (*S. aureus*) pathogens. The textural structures, morphological evolutions, and optical characteristics of the as-prepared samples were analyzed using advanced characterization techniques. X-ray diffraction confirmed the hexagonal phase of $Mg(OH)_2$ with improved crystallinity upon doping. Fourier transform infrared spectroscopy revealed $Mg(OH)_2$ stretching vibrations and other functional groups. UV−visible spectroscopy exhibited a red shift (bathochromic effect) in absorption spectra representing the decrease in energy band gap (E_g). Photoluminescence patterns were recorded to study recombination of charge carriers (e^- and h^+). A significant enhancement in photodegradation efficiency (97.62%) and efficient bactericidal actions against *E. coli* (14.10 mm inhibition zone) and *S. aureus* (7.45 mm inhibition zone) were observed for higher doped specimen 4% g-C_3N_4/St-$Mg(OH)_2$.

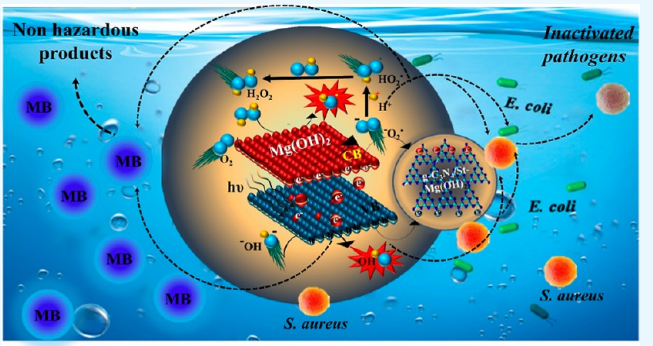

1. INTRODUCTION

In recent years, the continuously developing population and corresponding environmental deterioration caused by a substantial concentration of dyes, heavy metals, and microorganisms have become a serious concern of society and academia.[1] In developing countries, fast developments of industries give rise to industrial effluent removal into water bodies without appropriate precautions, endangering aquatic life and plant life. Specifically, organic dyes are toxic, carcinogenic, and potentially mutagenic, yet researchers do not break them down in the environment because of their structures. The significant human being's exposure to methylene blue (MB) through the food chain may cause dizziness, vomiting, shock, paralysis, cyanosis, and neurological injury in humans.[2,3] In addition, municipal wastewater is discharged into water reservoirs, and pathogens *Staphylococcus aureus* (*S. aureus*) and *Escherichia coli* (*E. coli*) in stagnant water storage pollute water.[4,5]

Hence, researchers must devise effective strategies to degrade hazardous contaminants. So far, different approaches have been employed, including physiochemical and biological approaches. The main issue is the high cost of these traditional treatment techniques on a wide scale. Moreover, these processes vary in effectiveness, cost, and environmental impact. Photocatalytic degradation utilizing renewable UV/sunlight is one of the auspicious water purification methods attributed to its simplicity, low cost, and lack of secondary pollutant production.[6] Photocatalysis begins with photoinduced e^- and h^+ on the catalyst's surface. Reactive oxygen species (ROS) are produced by employing photocatalysts along water vapors in aerobic circumstances. ROS are the highly reactive species that convert oxygen to O_2, $^{\bullet}O^{2-}$, H_2O_2, and $^{\bullet}OH$. Later, these

Received: July 22, 2022
Accepted: October 13, 2022
Published: October 24, 2022

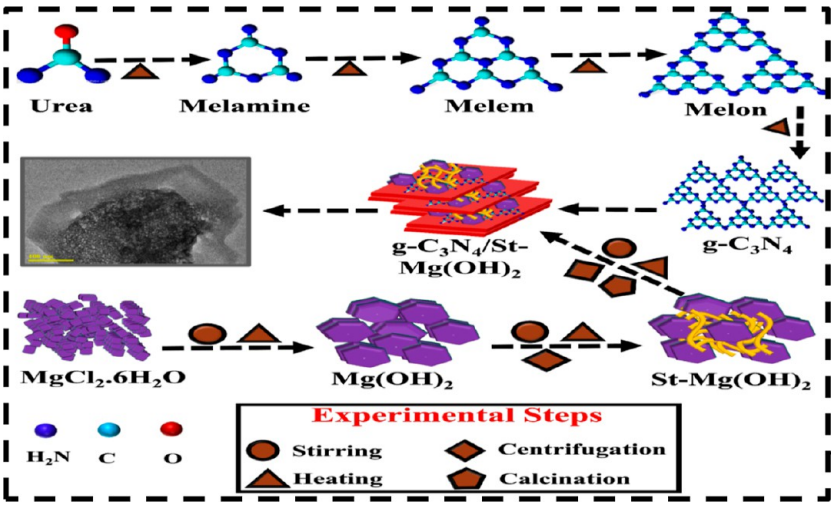

Figure 1. Schematic synthesis illustration of g-C_3N_4 by pyrolysis and g-C_3N_4/St-$Mg(OH)_2$ by co-precipitation.

described radicals degrade dyes and disturb bacterial cell membranes.[7,8]

Nanotechnology can be very helpful in supplying clean potable water for a growing population. Various photocatalysts, including oxides, sulfides, and halides, including TiO_2, ZnO, WO_3, MoS_2, ZnS, In_2S_3, AgCl, and BiOI, have been reported for hazardous pollutant remediation. However, the practical uses are restricted by swift electron−hole pair recombination, low quantum yields, and incredibly weak response to visible light.[9] Metal hydroxide-based nanomaterials such as $Ca(OH)_2$ and $Mg(OH)_2$ have been investigated as promising photocatalysts for MB dye decolorization. $Mg(OH)_2$ is found to be an eco-friendly, nonpoisonous, noncorrosive, and inexpensive photocatalyst and antibacterial agent for environmental decontamination. These applications are ascribed to the large surface area, biodegradability, and abundant hydroxyl (OH) groups on $Mg(OH)_2$ surfaces. Morphology and particle size significantly improve photocatalysis efficiency by permitting charge mobility, band gap modifications, surface reactivity, and adsorption. Various physiochemical methods were adopted to prepare $Mg(OH)_2$ nanostructures. Das et al. synthesized $Mg(OH)_2$ NPs using a precipitation route for the photodegradation of MB dye. Liu et al. synthesized $Mg(OH)_2$ nanoflowers using a hydrothermal route and exhibited the highest photocatalytic degradation against MB.[10−12] Moreover, positively charged $Mg(OH)_2$ also electrostatically attracts bacteria, degrades cell walls' integrity, and ultimately kills pathogens. The antibacterial process was also attributed to ROS formation, which disturbs membrane function and eventually kills bacteria[13,14] Pan et al. prepared $Mg(OH)_2$ nanoflakes as an antibacterial agent against *E. coli*. Kumari et al. prepared hexagonal $Mg(OH)_2$ sheets that exhibited bactericidal potential against pathogens (*S. aureus* and *E. coli*).[15] The co-precipitation process appears to be environmentally friendly and cost-effective, which allows modifying particle size distribution, surface area, morphology, and agglomeration. The described attributes rely mostly on the reaction temperature, pH, concentration, and type of reagent. Various morphologies, including hexagonal, rods, tubes, or needle-like, have been investigated using the co-precipitation synthesis route.[16] To strengthen the characteristics of nanomaterials, several methods such as tuning and doping with carbon-based substances and polymers have been proposed as a promising approach. By decreasing recombination probabilities of e^- and h^+, doping can significantly enhance photocatalytic activity (PCA).[17,18] Polymeric photocatalysts have been widely used to degrade water contaminants attributed to thermal stability, chemical inertness, and high surface areas. Various natural polymers such as chitin, chitosan, and starch have drawn great attention for environmental remediation.[19,20]

Starch is a highly abundant recyclable substance that has been extensively used for dye degradation because of the OH group in the polymer chain. Anionic starch has a high affinity to cationic dyes such as MB and crystal violet, introducing the carboxylate to improve selective adsorption performance.[21,22] Furthermore, 2D carbon-based material g-C_3N_4 has drawn great interest for water splitting as a photocatalyst, CO_2 reduction, pollutant remediation, and bacterial disinfection owing to its lower E_g, nontoxicity, physical stability, inexpensiveness, and chemical stability.[23,24] Peng and co-workers synthesized mesoporous C_3N_4 to adsorb MB from the aqueous environment.[25] Various metal (Zn, Cu, and Mg) hydroxides have been coupled with the g-C_3N_4 as highly effective photocatalysts for degradation performance by reducing charge carriers' recombination rate. Catalysts with required optical characteristics, large surface area, and stability may be produced by fabricating g-C_3N_4 with $Mg(OH)_2$. Therefore, to investigate the synergetic effect on dye degradation and bactericidal potential, polymers were doped with $Mg(OH)_2$.[26] The present study demonstrates a co-precipitation technique for synthesizing $Mg(OH)_2$ nanoparticles (NPs) and g-C_3N_4 layered nanosheets formed around St-$Mg(OH)_2$ NPs. The prepared samples have been used as photocatalysts for MB degradation from an aqueous solution. In addition, the bactericidal potential of prepared samples was also examined against *E. coli* and *S. aureus* via the agar diffusion technique.

2. EXPERIMENTAL SECTION

2.1. Materials. Magnesium chloride hexahydrate ($MgCl_2 \cdot 6H_2O$, 99%), starch $(C_6H_{10}O_5)_n$, sodium hydroxide (NaOH, 99%), and urea (CH_4N_2O, 99%) were acquired from Sigma-Aldrich, Germany.

2.2. Synthesis of g-C_3N_4 and Mg $(OH)_2$. To prepare g-C_3N_4, the usual procedure, that is, urea pyrolysis, was adopted.[27,28] Desired quantity of urea was heated in a furnace

https://doi.org/10.1021/acsomega.2c04650
ACS Omega 2022, 7, 39998−40008

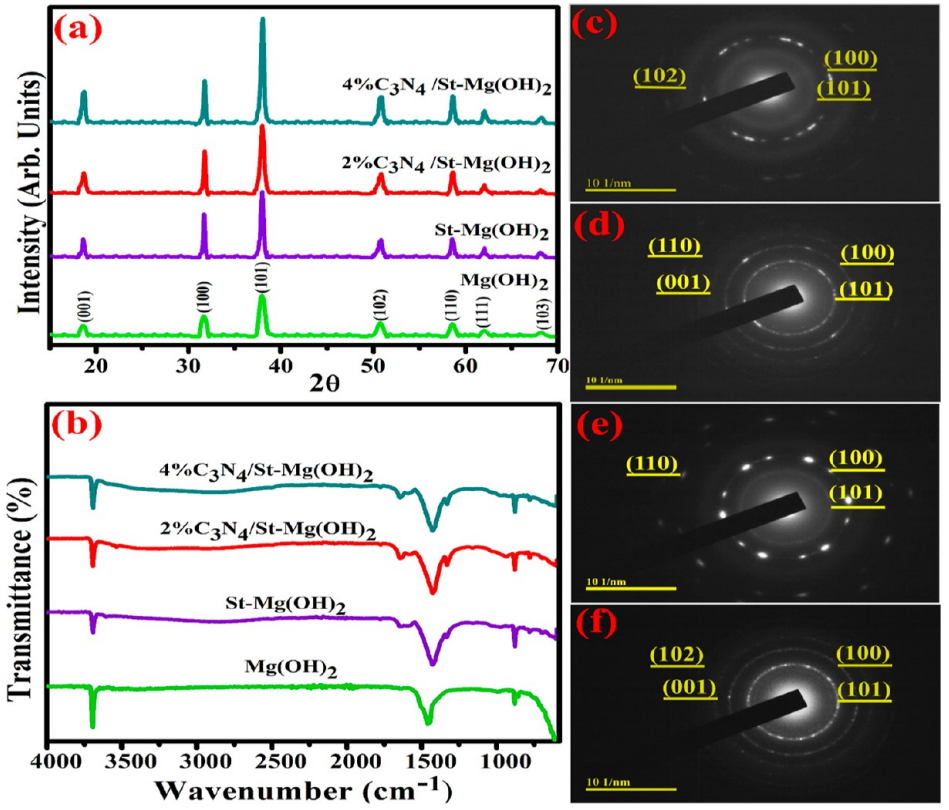

Figure 2. (a) XRD spectra of C_3N_4/St-$Mg(OH)_2$, (b) FTIR analysis, and (c–f) SAED pattern of $Mg(OH)_2$, St-$Mg(OH)_2$, and (g-C_3N_4/St-$MgOH)_2$.

at 500 °C for 5 h. Afterward, heating produced a schematic for possible intermediates at different temperature ranges forming melon, which was further heated to attain g-C_3N_4, as shown in Figure 1. $Mg(OH)_2$ was synthesized using 0.5 M $MgCl_2{\cdot}6H_2O$ through a co-precipitation technique under constant stirring at 100 °C. NaOH was incorporated as a precipitating agent into stirred solution, and precipitates appeared, indicating the formation of the compound. Afterward, the obtained sediment was centrifuged at 7500 rpm, dried at 200 °C for 12 h, and then crushed to collect the powder. Similarly, to prepare starch–$Mg(OH)_2$ and starch/g-C_3N_4–$Mg(OH)_2$, a fixed quantity of starch and various concentrations of g-C_3N_4 (0.02 and 0.04 wt %) were incorporated into $Mg(OH)_2$, as shown in Figure 1.

2.4. Photocatalysis Assay. MB dye was selected to evaluate the degradation potential of prepared samples. In a typical procedure, MB solution (5 mg/500 mL) was prepared in DI water and pH (4–12) was adjusted using NaOH and H_2SO_4 solutions to observe dye degradation in acidic and basic media. Afterward, 10 mg of synthesized samples was incorporated in 30 mL of MB solution and magnetically stirred in the dark to obtain adsorption–desorption equilibrium among photocatalysts and contaminants. Furthermore, the photocatalytic reaction was preceded for 120 min under a Hg lamp (400 W, 20 cm), and ∼3 mL of the irradiating suspension was excluded every 30 min. The optimum absorbance of MB was calculated before and after the light irradiation using the following degradation equation.

$$\text{Degradation } \% = (C_o - C_t)/C_o \times 100\ \% \quad (1)$$

where C_o and C_t correspond to MB concentrations before and after light irradiation, respectively.

2.5. Bactericidal Evaluation. In Punjab and Pakistan, mastitis-positive sheep milk samples were collected from neighborhood farms and veterinary clinics, refined on 5% blood agar (SBA), and matured at 37 °C for 24 h. Colonies were formed on McFarland on mannitol salt agar (MSA) and MacConkey (MA) in order to isolate Gram-positive (*S. aureus*) and Gram-negative (*E. coli*) bacteria, respectively. Gram staining and pharmacological (catalase and coagulase) methods were used to identify these specific colonies. A sterile cork borer was used under aseptic conditions to drill 6 mm-diameter wells on MSA and MA plates with varying sample doses into each well as the minimum and maximum (0.5 and 1.0 mg/0.05 mL) of pure and g-C_3N_4/starch-doped $Mg(OH)_2$. DI water (0.055 mL) and ciprofloxacin (0.005 mg/0.05 mL) were used as positive and negative controls, respectively. Furthermore, to determine antibacterial performance, the diameter of the inhibition zone was assessed using a Vernier caliper.

2.6. Radical Scavenging Assay. Free radical active species and antioxidant activity of the fabricated nanostructures were evaluated by a modified version of DPPH scavenging experiment. Pristine and g-C_3N_4–St-doped Mg-$(OH)_2$ NPs (25–300 μg/mL) were mixed with an equal volume of (0.1 mM) DPPH solution. This mixture was vortexed and incubated for 30 min at ambient temperature in the dark. A standard solution of ascorbic acid was employed as a reference sample. The degradation of DPPH solution (λ = 517 nm) was employed to calculate the scavenging rate (%) of each sample using eq 2

$$\text{Scavenging rate } (\%) = A_0 - A_1/A_0 \times 100 \quad (2)$$

https://doi.org/10.1021/acsomega.2c04650
ACS Omega 2022, 7, 39998–40008

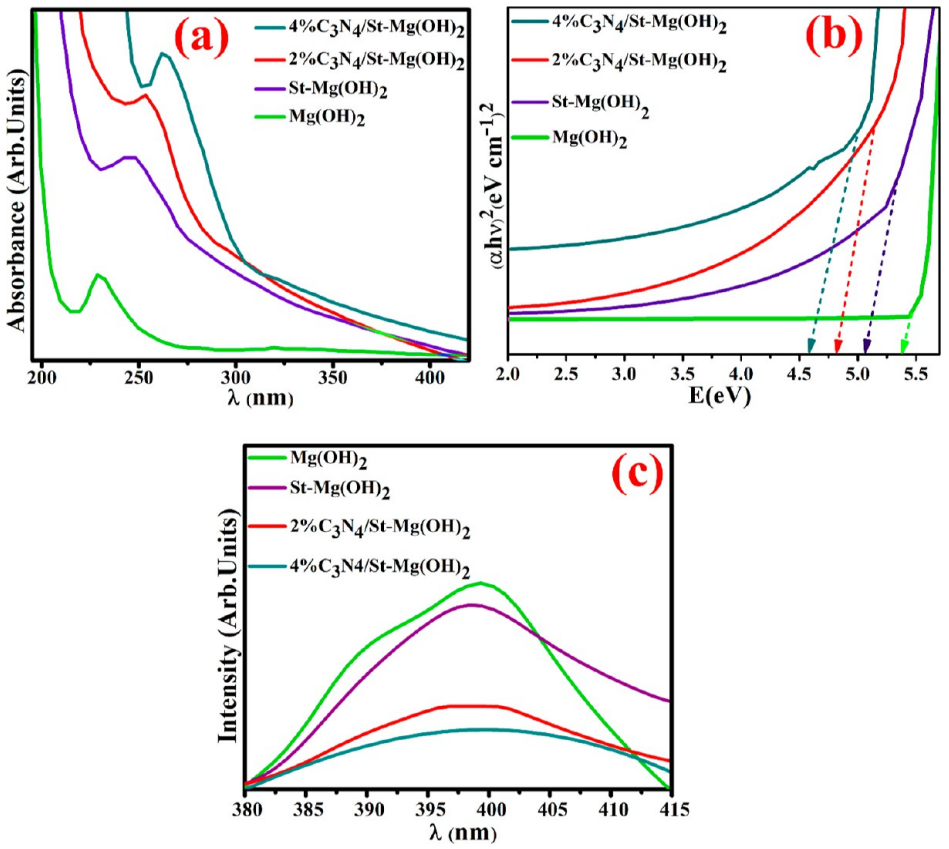

Figure 3. (a) Absorption spectra of C_3N_4/St-$Mg(OH)_2$ and (b) E_g and (c) PL spectra of synthesized samples.

Here, A_0 and A_1 represent control absorbance and standard absorbance, respectively.

2.7. Material Characterization Techniques. XRD with Cu Kα radiation (λ = 0.0154 nm and 2θ = 15−70°) was utilized to identify the crystal structure and phase of synthesized materials. Fourier transform infrared spectroscopy (FTIR) analyzed functional groups present in materials in the range 4000−580 cm^{-1}. Surface topography and interplanar spacing were inspected via energy-dispersive X-ray spectrometry and high-resolution transmission electron microscopy (HR-TEM, JEOL JEM 2100F). Absorbance spectra were determined using a UV−vis spectrophotometer (Genesys 10S) ranging from 195 to 420 nm. To elucidate photogenerated electron−hole pairs, recombination of prepared photocatalysts PL was employed.

3. RESULTS AND DISCUSSION

The phase composition, crystallinity, and lattice structure of $Mg(OH)_2$ and g-C_3N_4/St- $Mg(OH)_2$ were identified via XRD in the 10−70° range, Figure 2a. The peaks at 18.5° (001), 31.7° (100), 37.9° (101), 50.7° (102), 58.6° (110), 62° (111), and 68° (103) correspond to a hexagonal $Mg(OH)_2$ crystal reported in JCPDS no. 7−239. The sharp peaks confirm crystallinity, while broad peaks indicate the small particle size of $Mg(OH)_2$.[29] Furthermore, upon starch doping, crystallinity has been increased, revealing that $Mg(OH)_2$ crystals enhanced the crystallization by polymer matrixes.[13,30] Eventually, all the peaks were identified in pure and doped $Mg(OH)_2$ diffractograms without impurities. To access functional groups, FTIR spectral analysis was carried out, and related patterns were plotted among 4000−500 cm^{-1}, as illustrated in Figure 2b. Pure $Mg(OH)_2$ NP transmittance spectra were found around 3699, 1450, and 867 cm^{-1}, indicating O−H, C−O, and Mg−O/Mg−OH stretching vibrations correspondingly (see Figure 2b).[31−33] With starch doping, the transmittance peak appears at 1640 cm^{-1}, corresponding to intramolecular hydrogen bonding, indicating the existence of starch on the $Mg(OH)_2$ surface, while there was no discernible shift upon g-C_3N_4 doping.[34,35] The selected area electron diffraction (SAED) pattern was observed by directing electron beams on the sample lattice, revealing discrete diffraction rings and the crystalline structure of the synthesized samples, as illustrated in Figure 2c−f. Figure 2c,d reveals the polycrystalline nature of pure and St-$Mg(OH)_2$ NPs.[36] Figure 2e,f shows that upon 2% g-C_3N_4 doping, polycrystalline nature with a few bright spots appeared, while with 4% g-C_3N_4 doping, bright spots disappeared and displayed concentric circles.

A UV−vis spectrophotometer was employed to access optical characteristics in the λ = 200−430 nm range. As illustrated in Figure 3a, the optical absorption of $Mg(OH)_2$ indicates strong absorption peaks around 230 nm.[37] Absorption intensity mainly relies on particle size, charge carriers' concentration, and dielectric characteristics of the surrounding medium.[38] Upon doping, the absorption band is shifted toward the higher wavelength (230−260 nm) accompanied by the red shift. According to Figure 3b representation of Tauc's relation, the estimated band gap energy (E_g) of the $Mg(OH)_2$ sample was computed. E_g for $Mg(OH)_2$ was measured to be 5.4 eV,[13] and it was reduced to 4.6 eV for St/g-C_3N_4−$Mg(OH)_2$.

PL was carried out to elucidate photogenerated electron−hole pair recombination of prepared photocatalysts presented

https://doi.org/10.1021/acsomega.2c04650
ACS Omega 2022, 7, 39998−40008

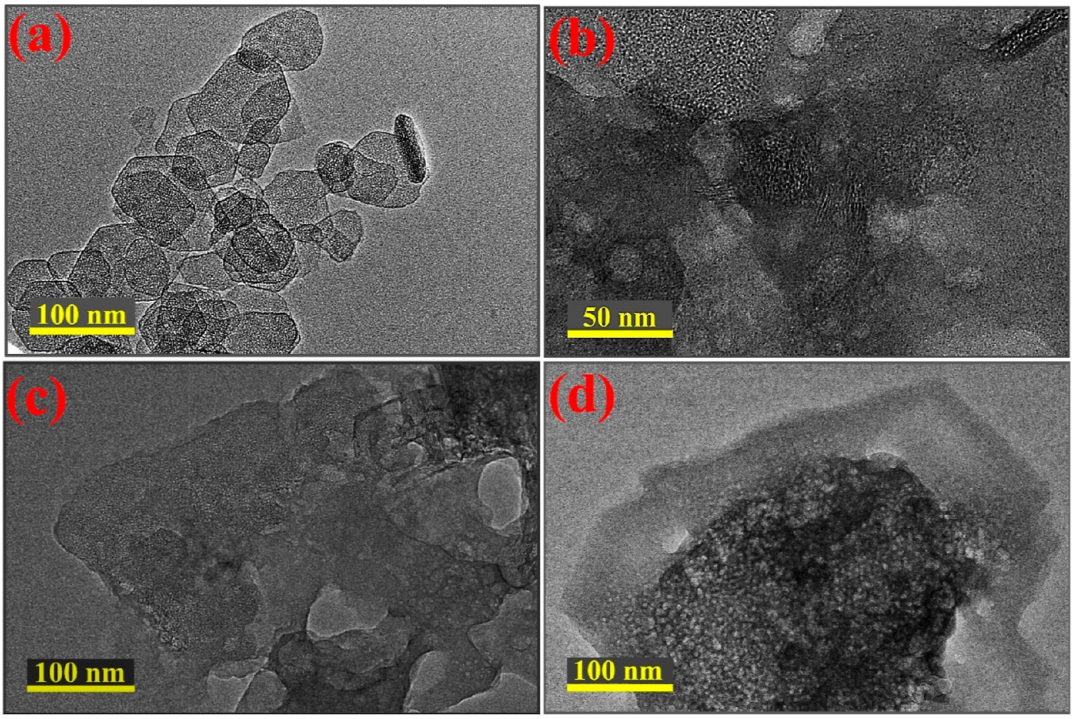

Figure 4. (a–d) TEM micrographs of (a) $Mg(OH)_2$ NPs, (b) St-$Mg(OH)_2$ NPs, and (c,d) 2 and 4% g-C_3N_4-loaded St-$Mg(OH)_2$ nanosheets.

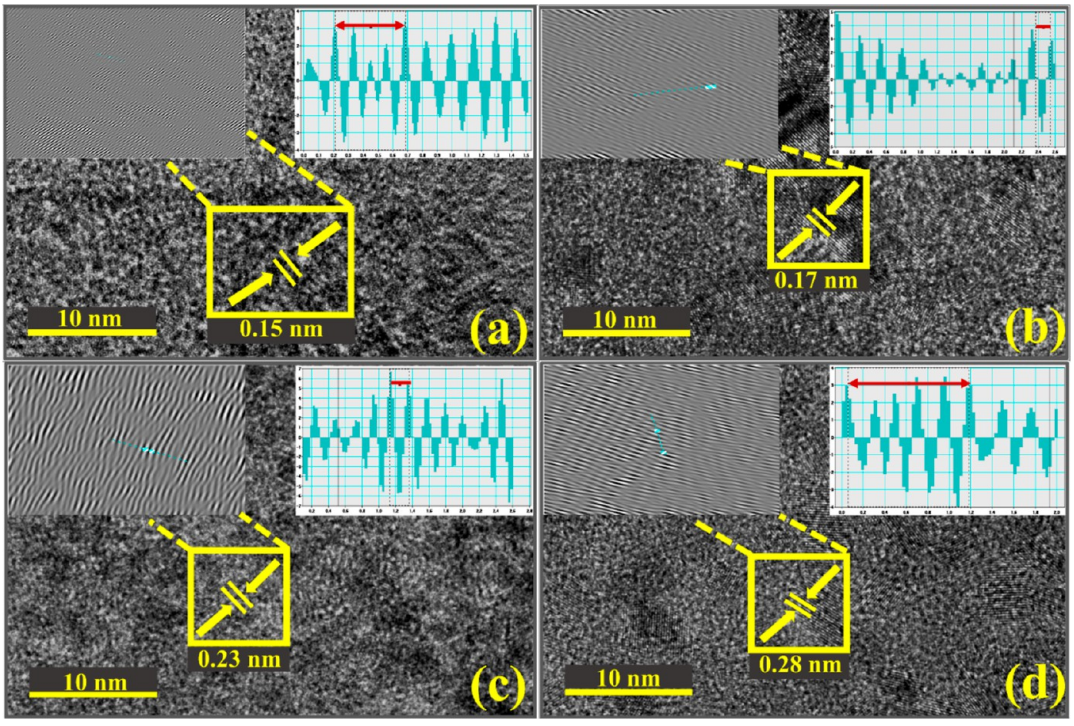

Figure 5. (a–d) HR-TEM images of pure and doped synthesized samples.

in Figure 3c. The strong and broad emission band was observed around 400 nm which was related to oxygen vacancies in $Mg(OH)_2$.[15,31] St-$Mg(OH)_2$ exhibits a decrease in emission intensity, while upon g-C_3N_4 doping, intensity reduction resulted in improving electron–hole separation due to the junction formed between the $Mg(OH)_2$ and g-C_3N_4.[26] These results reveal the enhanced degradation performance. Moreover, the emission band shape and position are the same except for intensity. This may be due to the same conditions under which all the nanomaterials were synthesized.

The morphology and surface topography of prepared samples were examined using TEM. Figure 4a reveals the randomly oriented hexagonal $Mg(OH)_2$ NPs. Figure 4b depicts the addition of starch and shows interpenetrated agglomeration that may be ascribed to the chemical compatibility between starch and $Mg(OH)_2$. The hydrogen bonding between the exposed OH group on the $Mg(OH)_2$

https://doi.org/10.1021/acsomega.2c04650
ACS Omega 2022, 7, 39998–40008

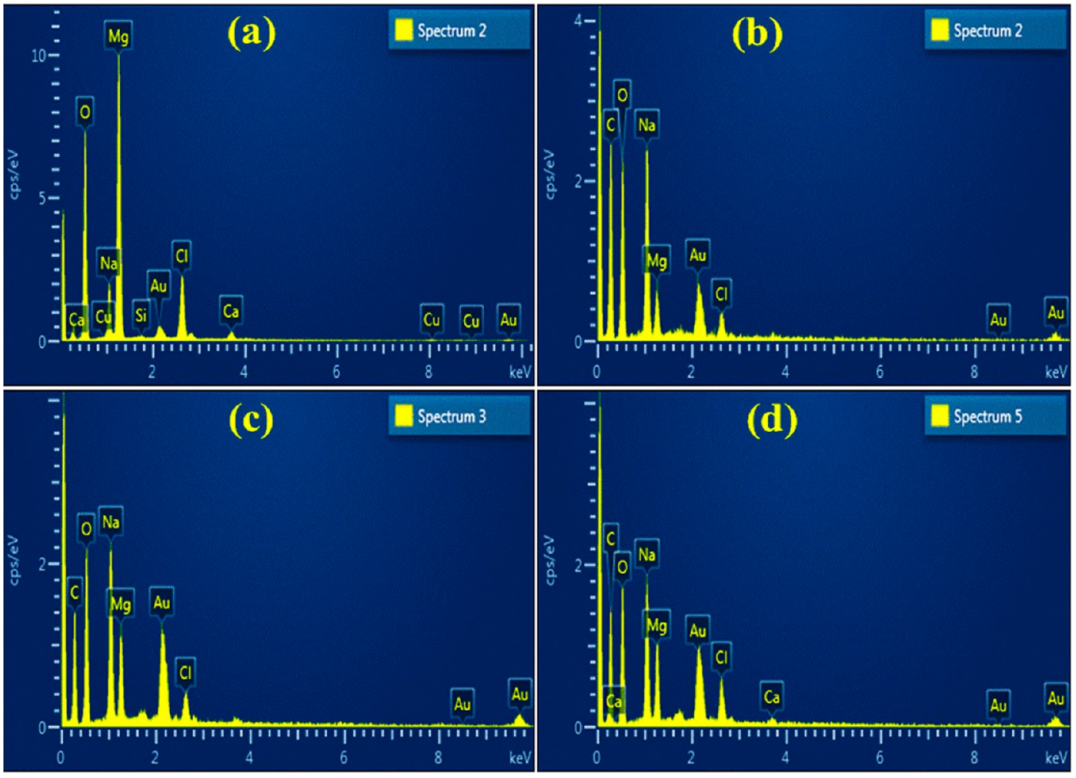

Figure 6. (a–d) EDS pattern of synthesized pure and g-C_3N_4/St-doped $Mg(OH)_2$ samples.

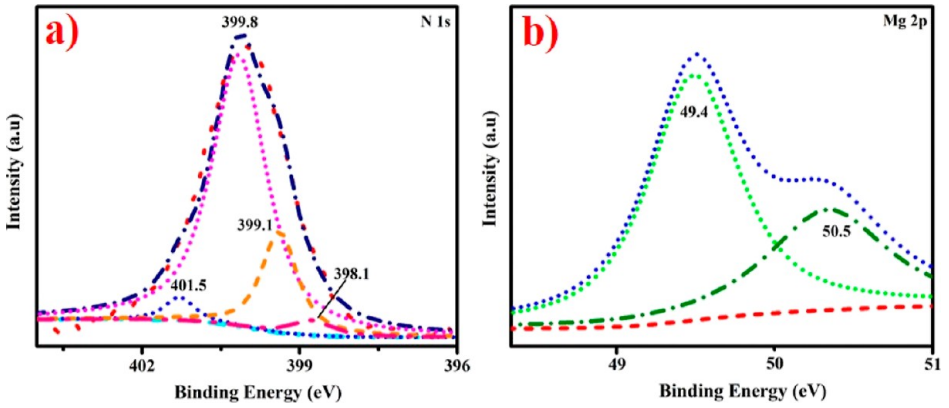

Figure 7. XPS spectra of fabricated g-C_3N_4/St-doped $Mg(OH)_2$ samples (a) N 1s and (b) Mg 2p.

surface and the starch macromolecules may cause the interfacial bonding. Figure 4c,d represents well-dispersed and wrapped St-$Mg(OH)_2$ NPs by layered structured g-C_3N_4 nanosheets. This may contribute to light absorption and the well-contact interaction of reactants with catalytic sites.

The lattice fringes of the synthesized product in the HR-TEM image are separated by an interplanar distance and calculated using Gatan software, as shown in Figure 5a–d. The pristine $Mg(OH)_2$ has an interlayer *d*-spacing of ∼0.15 nm (Figure 5a), compatible with the XRD result. Furthermore, adding polymers into $Mg(OH)_2$ shows considerable interplanar spacing from ∼0.15to 0.28 nm (Figure 5c,d).

The elemental composition of $Mg(OH)_2$ and St/g-C_3N_4–$Mg(OH)_2$ was assessed via EDS analysis. The results indicate that all elements present in the compound and the peaks of Mg, Cl, and O confirm the synthesis of $Mg(OH)_2$ from the $MgCl_2{\cdot}6H_2O$ precursor (Figure 6a–d). In addition, Cu, Na, and Au peaks were designated to the copper grid, used NaOH during synthesis as a precipitating agent, and gold coating.[39] The carbon peak may be attributed to St/g-C_3N_4 dopants.

XPS was used to investigate the elemental and surface composition and binding energy variations of g-C_3N_4/St-doped $Mg(OH)_2$ nanostructures, as represented in Figure 7a,b. The spectra of the N 1s core level indicate a wide peak positioned at 399.1 eV with a shoulder at greater BE. Deconvolution of data for fabricated nanostructures revealed four peaks with energies of 398.1, 399.1, 399.8, and 401.5 eV, separately. The predominant nitrogen signal, focused at 399.1 eV, is derived from the sp^2-bonded nitrogen in triazine rings (−C═NH). The peak at lower BE at 398.1 eV typically alludes to quaternary nitrogen, that is, "graphitic" nitrogen when nitrogen atom substitutes carbon in the graphene layer.[40] The bands at 399.8 and 401.5 eV correspond to tertiary nitrogen ($N-(C)_3$) and amino functional units containing

https://doi.org/10.1021/acsomega.2c04650
ACS Omega 2022, 7, 39998−40008

hydrogen atoms (C−N−H), respectively.[41,42] The Mg 2p spectrum comprised two peaks: one at 49.4 eV was corresponding to $Mg(OH)_2$ and $MgCO_3$,[43] while other at 50.5 eV was related to MgO.[44−47]

The photodegradation rate of organic dyes is significantly influenced by several parameters such as pH, concentration of dyes, photocatalyst particle size and its concentration, reaction temperature, and light intensity.[48] The pH alternation may shift the valence band (VB) and conduction band (CB) redox potentials and affect the interfacial charge transfer. The pH effect on PCA is generally attributed to electrostatic interaction among charges on the surface of the catalyst and dye molecule.[49] Figure 8 represents that initially, MB was not

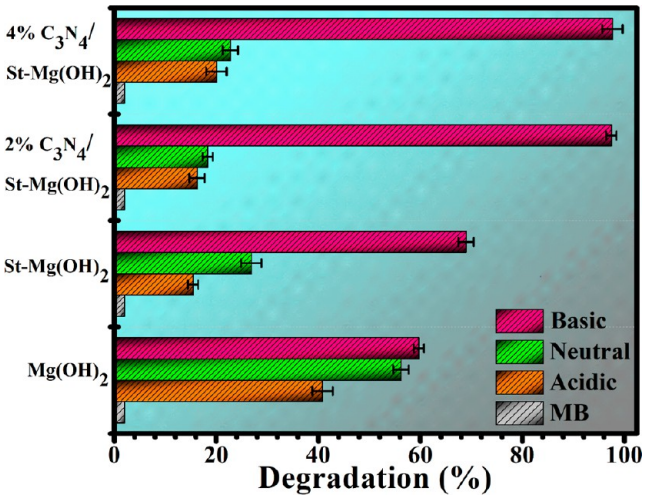

Figure 8. Degradation efficiency (%) of prepared pristine and g-C_3N_4−St-doped $Mg(OH)_2$ samples.

decolorized under light without catalysts, implying that MB has relative stability under irradiation. Therefore, MB dye was degraded with un-doped and doped $Mg(OH)_2$ photocatalysts showing 40.82, 15.45, 16.22, and 20.04% in acidic medium (pH = 4), 56.17, 26.87, 18.28, and 22.76% in neutral medium (pH = 7), and 59.69, 68.93, 97.42, and 97.62% in basic medium (pH = 12) correspondingly. It is clear that the pH degradation rate also increases because high pH encourages cationic MB dye adsorption on the catalyst surface. In the acidic medium, the positively charged $Mg(OH)_2$ catalyst tended to oppose cationic MB dye adsorption. In an alkaline medium, the catalyst's surface acquires a negative charge; therefore, dye degradation rate is enhanced. Similarly, the St-$Mg(OH)_2$ photocatalyst shows improved cationic dye degradation because in an alkaline medium, hydroxide ions could more readily attract starch and even ionize its protons, acquiring negative charges for starch molecules. Additionally, in higher doped specimen g-C_3N_4/St-$Mg(OH)_2$, superior photocatalytic efficacy can be ascribed to more active sites to enhance reaction provided by larger surface area.[26] Ge et al. synthesized g-C_3N_4/MgO nanosheets and found surface areas of 110.1 and 8.1 m^2/g for MgO and g-C_3N_4, respectively. The nanosheets of g-C_3N_4/MgO showed a synergetic effect for both cationic (MB) and anionic (methyl orange) dye degradation due to an increase in surface area.[50]

In this work, the results were compared with Degussa P25, and optimum MB dye degradation of 97.62% was observed for 4% g-C_3N_4/St-$Mg(OH)_2$. Degussa (Evonik) P25 is an extensively used titania photocatalyst that consists of 75% anatase and 25% rutile. Tichapondwa et al. performed MB degradation using Degussa (Evonik) P25 and obtained 81.4% degradation efficiency.[51,52]

A total organic carbon (TOC) assessment of treated water was conducted to estimate the dye (MB) degree of mineralization. The study was performed on St-$Mg(OH)_2$ and g-C_3N_4/St-$Mg(OH)_2$ (2 and 4%) using varying time intervals up to 120 min. This analysis (Figure 9) demonstrated

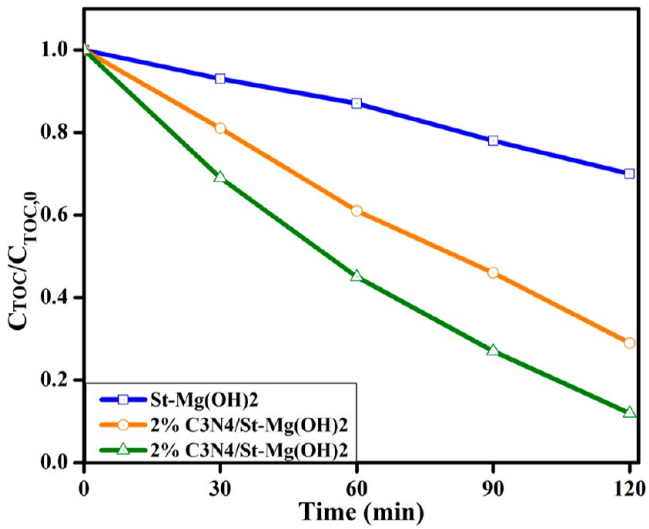

Figure 9. Variations in the TOC content of MB solution during photodegradation.

that the TOC of the MB solution treated with fabricated compounds under visible light irradiation reduced continuously with reaction time, and a significant amount of mineralization of the dye was found after 120 min in 4% g-C_3N_4/St-$Mg(OH)_2$. The study also indicates that the dye may be converted into various intermediate forms and that degradation of the dye after 120 min may culminate in its total mineralization.

In general, photocatalysis involves adsorption−desorption, e^- h^+ pair production, electron pair recombination, and chemical reaction.[53,54] The possible mechanism was described as follows to determine the degradation performance of $Mg(OH)_2$ NPs and the impact of ROS on the degradation of MB dye. PCA begins with irradiation of photon energy ($h\nu \geq E_g$) to excite electrons (e^-) from the lower VB to the upper CB, leaving behind a hole (h^+) in the VB (Figure 10). Under aqueous conditions, by the dissolution reabsorption process, Mg^{2+} species are generated (eq 2). MgOH formation is faster compared to ionization of $Mg(OH)_2$ (eq 3).

$$Mg(OH)_2 + h\nu \rightarrow Mg^{2+} + 2OH^- \quad (3)$$

$$Mg^{2+} + H^+ + 2OH^- \rightarrow MgOH + H_2O \quad (4)$$

Later, these formed e^- and h^+ react with O_2^- and OH^- to generate ROS, superoxide (O_2^-), and hydroxyl (OH*) radicals that can strongly oxidize organic dye (MB) into nonhazardous products (CO_2 and H_2O).

$$h^+_{VB} + OH^- \rightarrow OH^\bullet \quad (5)$$

$$e^-_{CB} + O_2^- \rightarrow O_2^\bullet \quad (6)$$

https://doi.org/10.1021/acsomega.2c04650
ACS Omega 2022, 7, 39998−40008

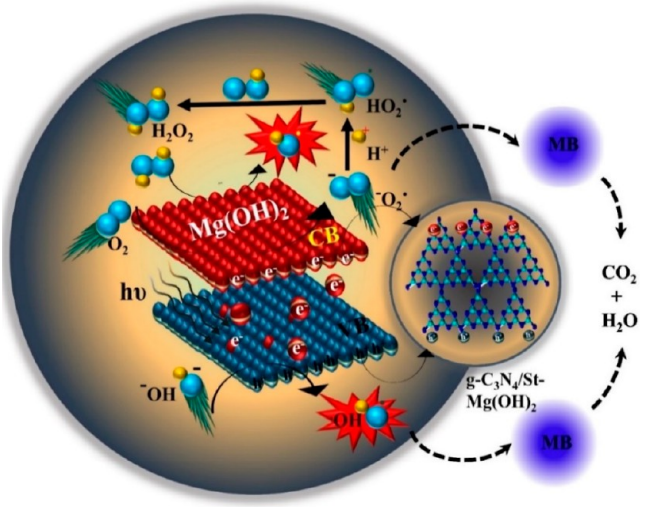

Figure 10. Photocatalysis mechanism of undoped and g-C_3N_4−St-doped $Mg(OH)_2$ nanostructures.

$$O_2^{\bullet} + H_2O \rightarrow HO_2^{\bullet} + OH^- \quad (7)$$

$$O_2^* + MB \rightarrow \text{Products } (CO_2 + H_2O) \quad (8)$$

$$OH^* + MB \rightarrow \text{Products } (CO_2 + H_2O) \quad (9)$$

$$H_2O_2 + e^- \rightarrow OH^* + OH^- \quad (10)$$

The results denoted that, in the photocatalytic oxidation of MB, OH* performs the main role compared to O_2*.[13]

The bactericidal behavior of pristine and doped $Mg(OH)_2$ nanostructures against *S. aureus* and *E. coli* was determined via the agar diffusion technique. At minimum and maximum concentration, significant zones of inhibition were seen as 1.55−4.10 mm and 2.05−7.45 mm for *S. aureus* and 1.45−7.05 mm and 1.80−14.10 mm for *E. coli* (Figure 11a,b). The results have been compared through DI water (0 mm) as the −ve control and ciprofloxacin as the +ve control with inhibitory areas (9.20 mm) for *S. aureus* and (14.35 mm) *E. coli*, as illustrated in Table 1. According to these observations, $Mg(OH)_2$ NPs show improved bactericidal performance toward *S. aureus* than *E. coli* because of the cell wall difference. This observation is attributed to the cell wall difference between G + ve and G − ve pathogens.[11] Upon starch and g-C_3N_4 doping into $Mg(OH)_2$, bactericidal potential enhanced toward *E. coli* gradually attributed to the thicker cell wall of *S. aureus* than *E. coli*.[55] Furthermore, (Figure 11c,d) shows that the % age efficacy of $Mg(OH)_2$ enhances upon doping for *S. aureus* as 16.84−44.56% and 22.28−80.97% at a minimum and higher concentrations, respectively. Similarly, the % age efficacy for *E. coli* also increases as 10.10−94.12% and 12.54−98.25% correspondingly.

The mechanistic antibacterial activity of the hexagonal $Mg(OH)_2$ is attributed to different types of NPS−bacteria interactions, including electrostatic interaction between the bacterial cell and NP surface, ROS generation attributed to oxygen vacancies on the surface of $Mg(OH)_2$ by redox reaction, and bacterial cell inactivation by cell membrane disruption and internal cellular leakage like; DNA, cytoplasm, and ribosomes resulting bacterial cell death, as shown in Figure 12.[11] In addition, the $Mg(OH)_2$ surface becomes alkaline because, in an alkaline environment, O_2^- and OH^- layers have high chemical stability.[56] DPPH scavenging was used to examine antioxidant effects of active radical species (Figure 13). Antioxidant activity of compounds is interrelated with their potential to transfer hydrogen or electrons to the DPPH

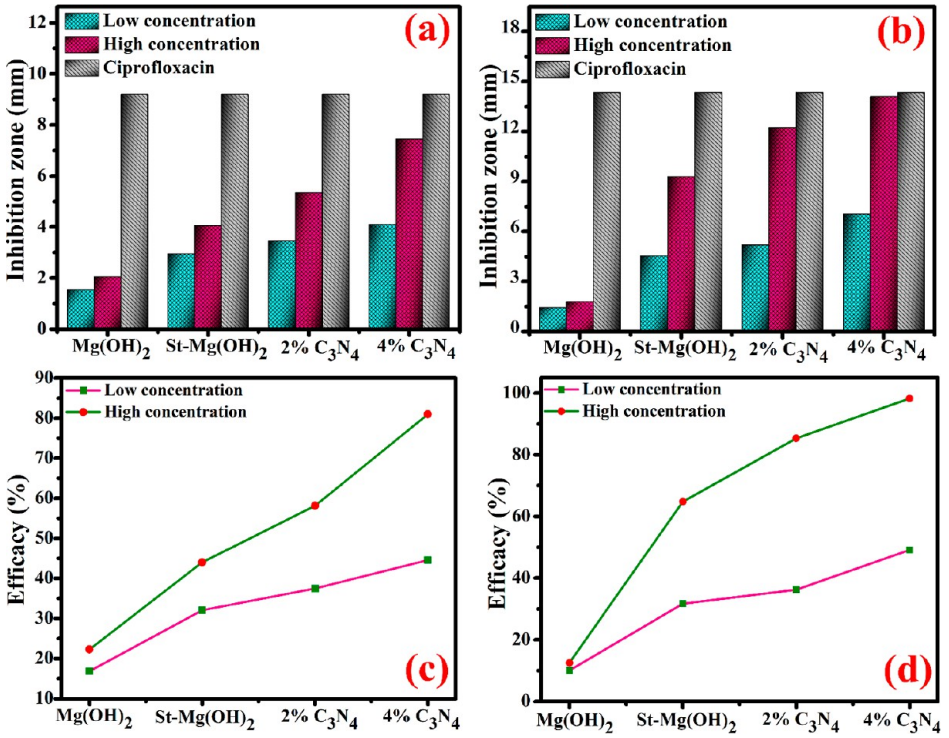

Figure 11. In vitro bactericidal potential of pure and g-C_3N_4/St-loaded $Mg(OH)_2$ against (a) *S. aureus* (b) *E. coli* and corresponding efficacy (%) for these bacteria in (c,d).

https://doi.org/10.1021/acsomega.2c04650
ACS Omega 2022, 7, 39998−40008

Table 1. Antibacterial Activity of Pristine and g-C_3N_4/St-Doped $Mg(OH)_2$

Samples	*S. aureus* inhibition region (mm)		*E. coli* inhibition region (mm)	
	0.5 mg/50 μL	1.0 mg/50 μL	0.5 mg/50 μL	1.0 mg/50 μL
$Mg(OH)_2$	1.55 ± 0.35	2.05 ± 1.15	1.45 ± 0.24	1.80 ± 0.46
St-$Mg(OH)_2$	2.95 ± 0.78	4.05 ± 1.27	4.55 ± 1.97	9.30 ± 3.12
2% g-C_3N_4/St-$Mg(OH)_2$	3.45 ± 1.34	5.35 ± 2.16	5.20 ± 2.10	12.25 ± 4.22
4% g-C_3N_4/St-$Mg(OH)_2$	4.10 ± 1.76	7.45 ± 2.94	7.05 ± 2.51	14.10 ± 4.92
Ciprofloxacin	9.20 ± 0.0	9.20 ± 0.0	14.35 ± 0.0	14.35 ± 0.0
DI water	0 ± 0.0	0 ± 0.0	0 ± 0.0	0 ± 0.0

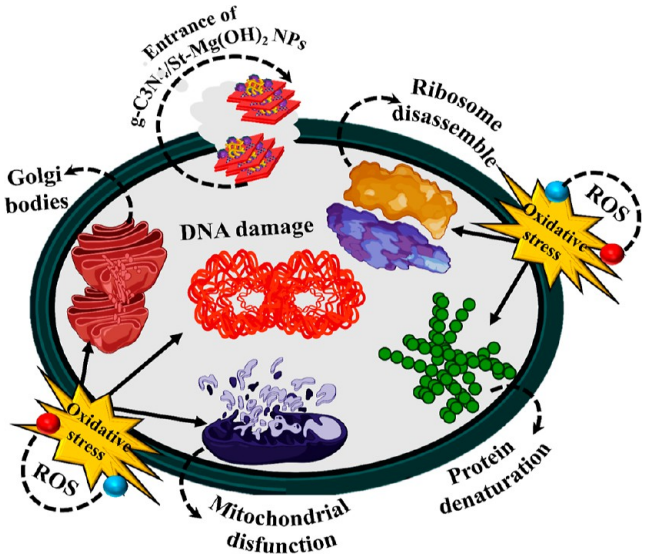

Figure 12. Bactericidal potential of pure and g-C_3N_4/St-loaded $Mg(OH)_2$.

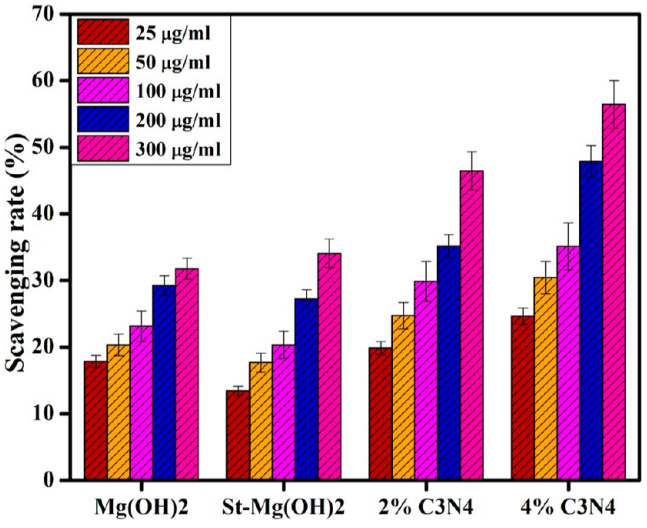

Figure 13. Antioxidant potential of pure and g-C_3N_4/St-loaded $Mg(OH)_2$.

free radical, resulting in stable diamagnetic compounds. All prepared samples exhibited a dose-dependent behavior; 4% g-C_3N_4/St-$Mg(OH)_2$ displayed the highest scavenging performance up to 56.45% at a 300 μg/mL concentration and scavenged DPPH radicals by donating hydrogen atoms. The formation of highly reactive $^{\bullet}OH$ and $^{\bullet}O_2$ radical species can interact with DPPH free radicals and result in bacterial cell death, which is highly correlated with the standard (ascorbic acid).

The comparison table of MB dye degradation and bactericidal action with the literature is shown in Table 2.

4. CONCLUSIONS

Novel pristine and g-C_3N_4/St-doped $Mg(OH)_2$ nanostructures were synthesized using the co-precipitation technique to examine photocatalytic and antibacterial activity. Several structural and optical characterization techniques were employed to examine the characteristics of synthesized nanostructures. The XRD pattern endorsed the hexagonal crystal structure of the pristine sample and improved crystallinity by incorporating dopants. Meanwhile, the presence of functional groups in synthesized NPs and metal hydroxide spectra was identified at 867 cm^{-1} using FTIR. TEM micrographs revealed hexagonal morphology of $Mg(OH)_2$ NPs. Polymers doping g-C_3N_4 and nanosheets wrapped around St-$Mg(OH)_2$ were investigated. Pure and doped $Mg(OH)_2$ exhibited interlayer spacing (0.15−0.28 nm), consistent with HR-TEM. EDS confirmed the elemental composition of pure and doped samples. UV spectra revealed that the red shift with doping led to gradually reduce E_g (5.4−4.6 eV). The efficiency of MB dye degradation implies the improved light-driven PCA upon polymer doping into $Mg(OH)_2$. Moreover, the agar diffusion technique assessed the bactericidal behavior of synthesized samples against *S. aureus* and *E. coli* pathogens. The optimum dye degradation efficiency (97.62%) and bactericidal solid action against *E. coli* (14.10 mm inhibition zone) was observed with incorporation of g-C_3N_4 into St-$Mg(OH)_2$. This research indicates that $Mg(OH)_2$ NPs with polymer doping might be environmentally and economically effective against pathogens and the dye degrader.

Table 2. Comparison Table of MB Degradation and Bactericidal Action with the Literature

materials	synthesis routes	MB degradation	antibacterial	references
$Mg(OH)_2$ sheets	precipitation	55%		13
$Mg(OH)_2$ flakes	co-precipitation		88% inhibition against *E. coli*	57
$Mg(OH)_2$ NPs	precipitation		6.5 mm*S. aureus* inhibition	58
4% C_3N_4/St-$Mg(OH)_2$	co-precipitation	97.62%	*S. aureus* inhibition (7.45 mm)and *E. coli*(14.10 mm)	present work

https://doi.org/10.1021/acsomega.2c04650
ACS Omega 2022, 7, 39998−40008

AUTHOR INFORMATION

Corresponding Authors

Muhammad Ikram − *Solar Cell Applications Research Lab, Department of Physics, Government College University Lahore, Lahore 54000, Pakistan;* orcid.org/0000-0001-7741-789X; Email: dr.muhammadikram@gcu.edu.pk

Walid Nabgan − *Departament d'Enginyeria Química, Universitat Rovira i Virgili, Tarragona 43007, Spain;* Email: walid.nabgan@urv.cat

Authors

Farzana Jamal − *Solar Cell Applications Research Lab, Department of Physics, Government College University Lahore, Lahore 54000, Pakistan*

Ali Haider − *Department of Clinical Sciences, Faculty of Veterinary and Animal Sciences, Muhammad Nawaz Shareef University of Agriculture, Multan 66000, Pakistan*

Sobia Dilpazir − *Department of Chemistry, Comsats University, Islamabad 45550, Pakistan*

Tahira Shujah − *Department of Physics, University of Central Punjab, Lahore 54000, Pakistan*

Misbah Naz − *Department of Chemistry, Division of Science & Technology, University of Education, Lahore 54000, Pakistan*

Muhammad Imran − *Department of Chemistry, Government College University Faisalabad, Sahiwal, Punjab 57000, Pakistan*

Anwar Ul-Hamid − *Core Research Facilities, King Fahd University of Petroleum & Minerals, Dhahran 31261, Saudi Arabia;* orcid.org/0000-0002-0259-301X

Iram Shahzadi − *Punjab University College of Pharmacy, University of the Punjab, Lahore 54000, Pakistan*

Hassam Ullah − *Department of Physics, Riphah Institute of Computing and Applied Sciences (RICAS), Riphah International University, Lahore 54000, Pakistan*

Salamat Ali − *Department of Physics, Riphah Institute of Computing and Applied Sciences (RICAS), Riphah International University, Lahore 54000, Pakistan*

Complete contact information is available at: https://pubs.acs.org/10.1021/acsomega.2c04650

Notes

The authors declare no competing financial interest.
Data available on demand.

ACKNOWLEDGMENTS

The authors are thankful to HEC, Pakistan via National Research Program for Universities (NRPU) project-20-17615.

REFERENCES

(1) Dang, X.; Yu, Z.; Yang, M.; Woo, M. W.; Song, Y.; Wang, X.; Zhang, H. Sustainable Electrochemical Synthesis of Natural Starch-Based Biomass Adsorbent with Ultrahigh Adsorption Capacity for Cr(VI) and Dyes Removal. *Sep. Purif. Technol.* **2022**, *288*, 120668.

(2) Li, Y.; Liu, S. J.; Chen, F. M.; Zuo, J. E. High-Strength Apatite/Attapulgite/Alginate Composite Hydrogel for Effective Adsorption of Methylene Blue from Aqueous Solution. *J. Chem. Eng. Data* **2019**, *64*, 5469−5477.

(3) Chen, L.; Zhu, Y.; Cui, Y.; Dai, R.; Shan, Z.; Chen, H. Fabrication of Starch-Based High-Performance Adsorptive Hydrogels Using a Novel Effective Pretreatment and Adsorption for Cationic Methylene Blue Dye: Behavior and Mechanism. *Chem. Eng. J.* **2021**, *405*, 126953.

(4) An, Y. J.; Kampbell, D. H.; Peter Breidenbach, G. Escherichia Coli and Total Coliforms in Water and Sediments at Lake Marinas. *Environ. Pollut.* **2002**, *120*, 771−778.

(5) Zheng, J. Inactivation of Staphylococcus Aureus in Water by Pulsed Spark Discharge. *Sci. Rep.* **2017**, *7*, 10311.

(6) Yaqoob, A. A.; Parveen, T.; Umar, K.; Mohamad Ibrahim, M. N. Role of Nanomaterials in the Treatment of Wastewater: A Review. *Water* **2020**, *12*, 495.

(7) Nosaka, Y.; Nosaka, A. Y. Generation and Detection of Reactive Oxygen Species in Photocatalysis. *Chem. Rev.* **2017**, *117*, 11302−11336.

(8) Taghizadeh, M. T.; Siyahi, V.; Ashassi-Sorkhabi, H.; Zarrini, G. ZnO, AgCl and AgCl/ZnO Nanocomposites Incorporated Chitosan in the Form of Hydrogel Beads for Photocatalytic Degradation of MB, E. Coli and S. Aureus. *Int. J. Biol. Macromol.* **2020**, *147*, 1018−1028.

(9) Freitas, F. S.; Gonçalves, A. S.; De Morais, A.; Benedetti, J. E.; Nogueira, A. F. Graphene-like MoS2 as a Low-Cost Counter Electrode Material for Dye-Sensitized Solar Cells. *J. NanoGe J. Energy Sustain.* **2012**, *1*, 11002−11003.

(10) Mathivanan, D.; Kirankumar, V. S.; Sumathi, S.; Suseem, S. R. Facile Biosynthesis of Calcium Hydroxide Nanoparticles Using Andrographis Echioides Leaf Extract and Its Photocatalytic Activity Under Different Light Source. *J. Cluster Sci.* **2018**, *29*, 167−175.

(11) Azzam, A. M.; Shenashen, M. A.; Selim, M. M.; Alamoudi, A. S.; El-Safty, S. A. Hexagonal $Mg(OH)_2$ Nanosheets as Antibacterial Agent for Treating Contaminated Water Sources. *ChemistrySelect* **2017**, *2*, 11431−11437.

(12) Liu, X.; Song, K.; Hu, J.; Tian, C.; Liu, W. Effective Destaining of Methylene Blue with Low Concentrations under Visible Light Irradiation in the Presence of $Mg(OH)_2$. *Surf. Interfaces* **2019**, *17*, 100219.

(13) Dharamalingam, K.; Ramasundaram, S.; Ponnusamy, V. K.; Bhuvaneswari, K.; Ramalingam, G.; Balasankar, A.; Jeyaram, S.; Pazhanivel, T.; Florence, S. S.; Thangavel, E.; Oh, T. H. Facile Synthesis of Polymer-Based Magnesium Hydroxide Nanocomposites for Photocatalytic Degradation for Methylene Blue Dye and Antibacterial Application. *Biomass Convers. Biorefin.* **2022**, 1−14.

(14) Wang, X. Y.; Hao, Y.; Zhao, H. B.; Guo, Y. R.; Pan, Q. J. 2D-Layered Mg(OH)2 Material Adsorbing Cellobiose via Interfacial Chemical Coupling and Its Applications in Handling Toxic Cd2+ and UO22+ Ions. *Chemosphere* **2021**, *279*, 130617.

(15) Kumari, L.; Li, W. Z.; Vannoy, C. H.; Leblanc, R. M.; Wang, D. Z. Synthesis, Characterization and Optical Properties of Mg(OH)2 Micro-/Nanostructure and Its Conversion to MgO. *Ceram. Int.* **2009**, *35*, 3355−3364.

(16) Calderón, D. J.; DeAlba-Montero, I.; Ruiz, F.; Echeverría, F. Effect of Synthesis Variables on the Characteristics of Magnesium Hydroxide Nanoparticles and Evaluation of the Fluorescence of Functionalised Mg(OH)2 Nanoparticles. *Adv. Nat. Sci.: Nanosci. Nanotechnol.* **2020**, *11*, 025008.

(17) Chanu, L. A.; Singh, K. J.; Devi, K. N. Study on the Photocatalytic Activity of Metal Oxide Nanoparticles towards the Degradation of Some Organic Dyes. *Integr. Ferroelectr.* **2020**, *204*, 90−99.

(18) Jorfi, S.; Pourfadakari, S.; Kakavandi, B. A New Approach in Sono-Photocatalytic Degradation of Recalcitrant Textile Wastewater Using MgO@Zeolite Nanostructure under UVA Irradiation. *Chem. Eng. J.* **2018**, *343*, 95−107.

(19) Saha, S.; Chaudhary, N.; Kumar, A.; Khanuja, M. Polymeric Nanostructures for Photocatalytic Dye Degradation: Polyaniline for Photocatalysis. *SN Appl. Sci.* **2020**, *2*, 1115.

(20) Yeamin, M. B.; Islam, M. M.; Chowdhury, A. N.; Awual, M. R. Efficient Encapsulation of Toxic Dyes from Wastewater Using Several Biodegradable Natural Polymers and Their Composites. *J. Cleaner Prod.* **2021**, *291*, 125920.

(21) Mallick, N.; Pal, D.; Soni, A. B.; Jhariya, D. C.; Singh, D. Starch Based Antimicrobial Food Packaging Film towards a Sustainable Environment. *IOP Conf. Ser.: Earth Environ. Sci.* **2020**, *597*, 012019.

https://doi.org/10.1021/acsomega.2c04650
ACS Omega 2022, 7, 39998−40008

(22) Hebeish, A. A.; Aly, A. A. Synthesis, Characterization and Utilization of Starch Hydroxypropyl Sulphate for Cationic Dye Removal. *Int. J. Org. Chem.* **2014**, *04*, 208−217.
(23) Zhang, Y.; Su, S.; Zhang, Y.; Zhang, X.; Giusto, P.; Huang, X.; Liu, J. Visible-Light-Driven Photocatalytic Water Disinfection Toward Escherichia Coli by Nanowired g-C3N4 Film. *Front. Nanotechnol.* **2021**, *3*, 3.
(24) Chen, Y.; Yu, Y.; Yan, Z.; Li, T.; Jing, Q.; Liu, P. Montmorillonite Induced Assembly of Multi-Element Doped g-C3N4 Nanosheets with Enhanced Activity for Rhodamine B Photodegradation. *Appl. Clay Sci.* **2022**, *218*, 106432.
(25) Peng, J.; Zhang, W.; Liu, Y.; Jiang, Y.; Ni, L.; Qiu, J. Superior Adsorption Performance of Mesoporous Carbon Nitride for Methylene Blue and the Effect of Investigation of Different Modifications on Adsorption Capacity. *Water, Air, Soil Pollut.* **2017**, *228*, 9.
(26) Gholami, P.; Khataee, A.; Vahid, B.; Karimi, A.; Golizadeh, M.; Ritala, M. Sonophotocatalytic Degradation of Sulfadiazine by Integration of Microfibrillated Carboxymethyl Cellulose with Zn-Cu-Mg Mixed Metal Hydroxide/g-C3N4 Composite. *Sep. Purif. Technol.* **2020**, *245*, 116866.
(27) Kharlamov, A.; Bondarenko, M.; Kharlamova, G.; Gubareni, N. Features of the Synthesis of Carbon Nitride Oxide (g-C3N4)O at Urea Pyrolysis. *Diamond Relat. Mater.* **2016**, *66*, 16−22.
(28) Paul, D. R.; Sharma, R.; Nehra, S. P.; Sharma, A. Effect of Calcination Temperature, PH and Catalyst Loading on Photo-degradation Efficiency of Urea Derived Graphitic Carbon Nitride towards Methylene Blue Dye Solution. *RSC Adv.* **2019**, *9*, 15381−15391.
(29) Munusamy, T. D.; Sarmin, S.; Ong, H. R.; Gan, W. T.; Hong, C. S.; Khan, M. M. R. Catalytic Performance and Antimicrobial Activity of Mg(OH)2/MgO Colloidal Nanoparticles in Alkyd Resin Nanocomposite Derived from Palm Oil. *Polym. Bull.* **2020**, *77*, 4571−4586.
(30) Piyada, K.; Waranyou, S.; Thawien, W. Mechanical, Thermal and Structural Properties of Rice Starch Films Reinforced with Rice Starch Nanocrystals. *Int. Food Res. J.* **2013**, *20*, 439−449.
(31) Yousefi, S.; Ghasemi, B.; Tajally, M.; Asghari, A. Optical Properties of MgO and Mg(OH)2 Nanostructures Synthesized by a Chemical Precipitation Method Using Impure Brine. *J. Alloys Compd.* **2017**, *711*, 521−529.
(32) Tlili, M.; Nefzi, C.; Alhalaili, B.; Bouzidi, C.; Ajili, L.; Jebbari, N.; Vidu, R.; Turki Kamoun, N. T. Synthesis and Characterization of Mgo Thin Films Obtained by Spray Technique for Optoelectronic Applications. *Nanomaterials* **2021**, *11*, 3076.
(33) Arshad, A.; Iqbal, J.; Siddiq, M.; Mansoor, Q.; Ismail, M.; Mehmood, F.; Ajmal, M.; Abid, Z. Graphene Nanoplatelets Induced Tailoring in Photocatalytic Activity and Antibacterial Characteristics of MgO/Graphene Nanoplatelets Nanocomposites. *J. Appl. Phys.* **2017**, *121*, 024901.
(34) Roy, J. S.; Pal Majumder, T.; Schick, C. Optical Characterization of CdS Nanorods Capped with Starch. *J. Mol. Struct.* **2015**, *1088*, 95−100.
(35) Rodriguez Llanos, J. H.; Tadini, C. C.; Gastaldi, E. New Strategies to Fabricate Starch/Chitosan-Based Composites by Extrusion. *J. Food Eng.* **2021**, *290*, 110224.
(36) Wang, Q.; Li, C.; Guo, M.; Sun, L.; Hu, C. Hydrothermal Synthesis of Hexagonal Magnesium Hydroxide Nanoflakes. *Mater. Res. Bull.* **2014**, *51*, 35−39.
(37) Hanlon, J. M.; Bravo Diaz, L.; Balducci, G.; Stobbs, B. A.; Bielewski, M.; Chung, P.; MacLaren, I.; Gregory, D. H. Rapid Surfactant-Free Synthesis of Mg(OH)2 Nanoplates and Pseudomorphic Dehydration to MgO. *CrystEngComm* **2015**, *17*, 5672−5679.
(38) Bhargava, R.; Khan, S. Effect of Reduced Graphene Oxide (RGO) on Structural, Optical, and Dielectric Properties of Mg(OH)-2/RGO Nanocomposites. *Adv. Powder Technol.* **2017**, *28*, 2812−2819.
(39) Alaizeri, Z. M.; Alhadlaq, H. A.; Aldawood, S.; Akhtar, M. J.; Amer, M. S.; Ahamed, M. Facile Synthesis, Characterization, Photocatalytic Activity, and Cytotoxicity of Ag-Doped Mgo Nanoparticles. *Nanomaterials* **2021**, *11*, 2915.
(40) Lahoud, A.*Post-Traumatic Urbanism*; Wiley, 2010; Vol. *80*, pp 14−23.
(41) Sun, Y.; Li, C.; Xu, Y.; Bai, H.; Yao, Z.; Shi, G. Chemically Converted Graphene as Substrate for Immobilizing and Enhancing the Activity of a Polymeric Catalyst. *Chem. Commun.* **2010**, *46*, 4740−4742.
(42) Xiang, Q.; Yu, J.; Jaroniec, M. Preparation and Enhanced Visible-Light Photocatalytic H2- Production Activity of Graphene/C3N4 Composites. *J. Phys. Chem. C* **2011**, *115*, 7355−7363.
(43) Unocic, K. A.; Elsentriecy, H. H.; Brady, M. P.; Meyer, H. M.; Song, G. L.; Fayek, M.; Meisner, R. A.; Davis, B. Transmission Electron Microscopy Study of Aqueous Film Formation and Evolution on Magnesium Alloys. *J. Electrochem. Soc.* **2014**, *161*, C302−C311.
(44) Chong, K. Z.; Shih, T. S. Conversion-Coating Treatment for Magnesium Alloys by a Permanganate-Phosphate Solution. *Mater. Chem. Phys.* **2003**, *80*, 191−200.
(45) Chen, S.; Yan, F.; Xue, F.; Yang, L.; Liu, J. X-Ray Photoelectron Spectroscopy Investigations of Zinc-Magnesium Alloy Coated Steel. *Mater. Chem. Phys.* **2010**, *124*, 472−476.
(46) Zhang, Y.; Shao, Y.; Zhang, T.; Meng, G.; Wang, F. The Effect of Epoxy Coating Containing Emeraldine Base and Hydrofluoric Acid Doped Polyaniline on the Corrosion Protection of AZ91D Magnesium Alloy. *Corros. Sci.* **2011**, *53*, 3747−3755.
(47) Ko, Y. G.; Namgung, S.; Shin, D. H. Correlation between KOH Concentration and Surface Properties of AZ91 Magnesium Alloy Coated by Plasma Electrolytic Oxidation. *Surf. Coat. Technol.* **2010**, *205*, 2525−2531.
(48) Reza, K. M.; Kurny, A.; Gulshan, F. Parameters Affecting the Photocatalytic Degradation of Dyes Using TiO2: A Review. *Appl. Water Sci.* **2017**, *7*, 1569−1578.
(49) Kong, J. Z.; Li, A. D.; Li, X. Y.; Zhai, H. F.; Zhang, W. Q.; Gong, Y. P.; Li, H.; Wu, D. Photo-Degradation of Methylene Blue Using Ta-Doped ZnO Nanoparticle. *J. Solid State Chem.* **2010**, *183*, 1359−1364.
(50) Ge, L.; Peng, Z.; Wang, W.; Tan, F.; Wang, X.; Su, B.; Qiao, X.; Wong, P. K. g- C_3N_4/MgO Nanosheets: Light-Independent, Metal-Poisoning-Free Catalysts for the Activation of Hydrogen Peroxide to Degrade Organics. *J. Mater. Chem. A* **2018**, *6*, 16421−16429.
(51) Abou-Gamra, Z. M.; Ahmed, M. A. Synthesis of Mesoporous TiO2-Curcumin Nanoparticles for Photocatalytic Degradation of Methylene Blue Dye. *J. Photochem. Photobiol., B* **2016**, *160*, 134−141.
(52) Tichapondwa, S. M.; Newman, J. P.; Kubheka, O. Effect of TiO2 Phase on the Photocatalytic Degradation of Methylene Blue Dye. *Phys. Chem. Earth* **2020**, *118-119*, 102900.
(53) Ananpattarachai, J.; Kajitvichyanukul, P.; Seraphin, S. Visible Light Absorption Ability and Photocatalytic Oxidation Activity of Various Interstitial N-Doped TiO2 Prepared from Different Nitrogen Dopants. *J. Hazard. Mater.* **2009**, *168*, 253−261.
(54) Muñoz-Batista, M. J.; Luque, R. Heterogeneous Photocatalysis. *ChemEngineering* **2021**, *5*, 26.
(55) Kanth, S.; Puttaiahgowda, Y. M.*Current State and Future Perspectives of Starch Derivatives and Their Blends as Antimicrobial Materials. Starch/Staerke*; John Wiley and Sons Inc, 2022; Vol. *74*.
(56) Wang, Y.; Sha, L.; Zhao, J.; Li, Q.; Zhu, Y.; Wang, N. Antibacterial Property of Fabrics Coated by Magnesium-Based Brucites. *Appl. Surf. Sci.* **2017**, *400*, 413−419.
(57) Pan, X.; Wang, Y.; Chen, Z.; Pan, D.; Cheng, Y.; Liu, Z.; Lin, Z.; Guan, X. Investigation of Antibacterial Activity and Related Mechanism of a Series of Nano-Mg(OH)2. *ACS Appl. Mater. Interfaces* **2013**, *5*, 1137−1142.
(58) Vatsha, B.; Tetyana, P.; Shumbula, P. M.; Ngila, J. C.; Sikhwivhilu, L. M.; Moutloali, R. M. Effects of Precipitation Temperature on Nanoparticle Surface Area and Antibacterial Behaviour of $Mg(OH)_2$ and MgO Nanoparticles. *J. Biomater. Nanobiotechnol.* **2013**, *04*, 365−373.

https://doi.org/10.1021/acsomega.2c04650
ACS Omega 2022, 7, 39998−40008